Electronic Supplementary Information

Dominating (111) Facets with ordered stacking in Perovskite Films

Xiaotao Liu,[ab] Xiaoqing Jiang,[b] Yanfeng Yin,[d] Jiafeng Zhang,[bc] Hao Tian,[bc] Junxue Guo,[b] Xin Guo,*[bc] Can Li*[bc]

[a] School of Materials Science and Engineering & National Institute for Advanced Materials, Nankai University, Tongyan Road 38, Tianjin, 300350, China.

[b] Key Laboratory of Photoelectric Conversion and Utilization of Solar Energy, State Key Laboratory of Catalysis, Dalian National Laboratory for Clean Energy, Dalian Institute of Chemical Physics, Chinese Academy of Sciences, Zhongshan Road 457, Dalian, 116023, China.

[c] University of Chinese Academy of Sciences, Beijing 100049, China.

[d] State Key Laboratory of Molecular Reaction Dynamics and the Dynamic Research Center for Energy and Environmental Materials, Dalian Institute of Chemical Physics, Chinese Academy of Sciences, Zhongshan Road 457, Dalian, 116023, China.

* E-mail: guoxin@dicp.ac.cn; canli@dicp.ac.cn

Experimental Section

Materials

Tin (IV) oxide-SnO_2 (15% in H_2O colloidal dispersion) was purchased from Alfa Aesar. Isopropanol (IPA, 99.5%), N, N-dimethylformamide (DMF, 99.8%), dimethyl sulfoxide (DMSO, 99.7%) and chlorobenzene (CB, 99.8%) were purchased from Sigma Aldrich. Formamidine iodide (FAI), methylammonium iodide (MAI), methylammonium chloride (MACl), *n*-butylammonium iodide (BAI), *n*-butylammonium acetate (BAAc), 4-fluoro-phenethylammonium iodide (FPEAI), lead iodide (PbI_2, 99.999%), 4-tert-butylpyridine (TBP), bis(trifluoromethylsulfonyl)imide lithium salt (Li-TFSI), and spiro-OMeTAD (99.5%) were purchased from Xi'an Polymer Light Technology Corp.

Device fabrication and characterization

Preparation for solution: For the PbI_2 precursor solution, the PbI_2 (1.45 M) is dissolved in DMF/DMSO (V:V = 910:90), which is stirred at 70 °C for 2 h before use. For the organic ammonium salt-containing PbI_2 precursor solutions, PEAI, OAI, BAI and BAAc are, respectively, added with an optimized molar ratio of 3% relative to PbI_2. The solution of FAI:MAI:MACl (180 mg:13 mg:18 mg in 2 mL IPA) for the second step is stirred at room temperature for 2 h.

Device fabrication: Patterned ITO glasses were cleaned sequentially by aqueous detergent, de-ionized water, ethanol for 20 min each step, then treated by UV-ozone for 20 min before use. The SnO_2 precursor solution (volume ratio of SnO_2 colloidal solution to the deionized water of 1:4) was spin-casted onto ITO glasses at 4000 r.p.m.

for 30 s, followed by annealed at 150 °C for 30 min under ambient atmosphere. SnO_2 films were treated by UV-ozone for 20 min before spin-coating PbI_2. Then, the substrate was transferred to a glove box filled with N_2 atmosphere. PbI_2 precursor solutions were spin-coated at 1500 r.p.m. for 30 s, then annealed at 70 ^oC for 1 min in glove box. Next, FAMA precursor solution was spin-coated on PbI_2 films with 2100 r.p.m. for 30 s in glove box, which were annealed at 150 °C for 15 min in ambient environment with 30%-40% relative humidity. The FPEAI solution (5 mg/mL) was spin-coated on the surface of perovskite film (3000 rpm for 30 s). The spiro-OMeTAD precursor solution (72.3 mg/mL) with 29 μL of TBP, 17.5 μL of LiTFSI (520 mg/mL) was spin-coated onto the perovskite film at 3000 r.p.m. for 30 s. Finally, Au (100 nm) were deposited on the surface of HTL by thermal evaporator with high vacuum ($<7 \times 10^{-4}$ Pa).

Instrumentations and characterizations

UV–vis absorption spectra for films were measured with SHIMADZU-UV-1750. XRD (TD-3500X) with Cu Kα radiation was used to measure the crystal structure of perovskite films. The GIWAXS patterns were measured at BL14B1 beamline, Shanghai Synchrotron Radiation Facility (SSRF). The morphology of films was acquired with the SEM (SU8010). Photoluminescence (PL) spectra and time-resolved photoluminescence (TRPL) decay curves wer measured by a FLSP920 spectrometer (Edinburgh Instruments). Kelvin probe force microscopy (KPFM) was implemented by using a Bruker Dimension VSPM system. Electrochemical impedance spectroscopy (EIS) measurements were performed by the Zahner electrochemical

workstation (CHI600D) with the frequency range of 100000 Hz to 1 Hz in a bias of 0.9 V under dark condition. To calculate the trap density (N_t), the space-charge limited current (SCLC) measurements were conducted using an electron-only devices with a structure of ITO/SnO_2/perovskite/FPEAI/PCBM/Ag to obtain the onset voltage of TFL (V_{TFL}) with the formula:

$$N_t = \frac{2V_{VTL}\varepsilon_r\varepsilon_0}{qL^2},$$

where the ε_r, q, L, and ε_0 represented dielectric constant, elementary charge, thickness of the perovskite films, and the vacuum permittivity, respectively. Current–voltage (*J-V*) curves of the corresponding devices were measured at a scan rate of 0.02 V/s by a Keithley 2400 source meter with an Enlitech SS-F5-3A solar simulator (Enli Tech, Taiwan) in ambient condition at room temperature (25 ± 5 °C/30-35 % relative humidity) based on a shadow mask with 0.05 cm^2 aperture. The light intensity was calibrated to AM 1.5 G solar light condition of 100 mW cm^{-2} using the certified silicon solar cell (Newport 532 ISO1599). The external quantum efficiency (EQE) spectra were got by a solar-cell spectral-response measurement system (QE-R, Enlitech). The humidity stability test was conducted in ambient environment at 20-35 °C with 40%-50% relative humidity. The light stability was tested under continuous illumination (100 mW·cm^{-2}) in glove box with N_2 atmosphere. The HRTEM images of perovskite films were acquired using a TEM (JEM-2100). The Mott-Schottky plots were obtained by an electrochemical workstation (IVIUMSTAT) with an applied voltage range from 0 V to 1.5 V. Depth profiling data of ion distribution was obtained by the ToF-SIMS (M6, IONTOF GmbH). Bi^{3+} ions with a 30 keV were used as

primary ions beam for an analysis area of 50 μm x 50 μm. Sputtering was performed with a raster size of 200 μm×200 μm.

Analysis of diffusion coefficient (D): The carrier diffusion of perovskite films can be determined using a three-dimensional diffusion model:[1]

$$\frac{\partial \emptyset(x,y,z,t)}{\partial t} = D\left\{\frac{\partial^2 \emptyset(x,y,z,t)}{\partial x^2} + \frac{\partial^2 \emptyset(x,y,z,t)}{\partial y^2} + \frac{\partial^2 \emptyset(x,y,z,t)}{\partial z^2}\right\} - k_1 \emptyset(x,y,z,t) - k_2 \emptyset(x,y,z,t) \quad (1)$$

where ϕ(x,y,z,t) is the concentration of charge carriers (time t) of the position (x,y,z), D is the diffusion coefficient, k_1, k_2 represent the first-order and second-order recombination coefficient, respectively. To avoid a high order recombination process, we carried out the PL imaging measurements at a low excitation intensity.

The PL intensity images reflect the distribution of photogenerated carriers along the lateral (2D) dimension within the perovskite film. After excitation (t = 0), the carrier distribution along the crystal depth direction (z-direction) follows the absorption optical depth profile. The transport of carriers along the z-direction should not affect their distribution in the lateral dimension. Therefore, the carrier distribution in the lateral dimension at a delay time t (using a Gaussian excitation beam) can be described by 2D Gaussian function:[2]

$$n(x,y,t) = Nexp\left[-\frac{(x-x_0)^2}{2\sigma_{t\,x}^2} - \frac{(y-y_0)^2}{2\sigma_{t,y}^2}\right] \quad (2)$$

and the PL intensity distribution I_{PL} (x, y, t) is

$$I_{PL}(x,y,t) \propto n(x,y,t) \quad (3)$$

Herein, x_0 and y_0 are the initial position of Gaussian excitation beam; $\sigma^2_{t,x}$ and $\sigma^2_{t,y}$ are the time-dependent Gaussian deviation along x and y direction. The transport of exciton results in the variation of σ^2 at different delay times. To quantitatively determine the transport parameters, we extracted the 1D PL intensity profiles at the maximum intensity cross sections in the PL images. In these 1D profiles, the exciton transport process can be exhibited by the broadening of the distribution peak (σ) as the delay increases. On the basis of previously reported 1D diffusion model,[2] the Gaussian variance σ is directly related to exciton diffusion coefficient (D) by

$$\sigma_{t,x}^2 = \sigma_{0,x}^2 + l^2 = \sigma_{0,x}^2 + 2Dt \tag{4}$$

where $l = 2(Dt)^{1/2}$, representing the distance of carrier spreading out (along +x and –x directions) from initial position. Thus, a linear fit of the measured Gaussian variance as a function of time directly yields the diffusion coefficient D by:

$$D = \frac{\sigma_x^2(t) - \sigma_{0,x}^2}{2t} \tag{5}$$

Photoluminescence scanned imaging microscopy: The PL kinetics within the perovskite film was mapped by a home-built photoluminescence (PL)-scanned imaging microscope coupled with a time-correlated single photon counting (TCSPC) module. Excitation of the sample was carried by a pulse laser (PIXEA-CU-1, AUREA, France) of 406 nm wavelength, 5 MHz repetition rate and ~35 ps pulse width. The excitation laser beam focused on the sample through a 100× air objective lens (NA = 0.95, Olympus SLMPlan N, 100 X) with the spot radius of 1.02 μm ($1/e^2$ of the maximum intensity measured with a EMCCD camera, DU-897U-CS0-#BV, Andor, UK). By parking the excitation laser spot in a specific position of the perovskite film,

fast scanning of the galvanometer mirror ensures to collect photons emission from the whole SC. Each scanning image includes 256 × 256 pixels. The fluorescence signal was collected with a high-speed detector (HPM-100-50, Hamamatsu, Japan) with a 460 nm long pass filter.

Computational Methods: Density functional theory (DFT) calculations on the adsorption energy were conducted using the Vienna Ab initio Simulation Package (VASP).[3] The projected augmented wave (PAW) method[4] and the Perdew-Burke-Ernzerhof (PBE)[5] functional within the generalized gradient approximation (GGA) were used to describe the interaction between ion-cores and valence electrons and exchange-correlation effects, and the system's energy cutoff of 450 eV (with per unit cell's energy cut value of 55.43 eV) was applied for the plane-wave function expansion. The van der Waals (vdW) dispersion interactions between the perovskite facets and BA^+/FA^+ reaction intermediates were described using the DFT-D3 correction.[6] The Brillouin zones were sampled using the 3×3×1 uniform *k* point mesh. The atomic positions of all slabs were relaxed until total energy changes were below 10^{-4} eV, and the maximum force was reduced to 0.02 eV A^{-1}.

The adsorption energy (E_{ads}) is defined as $E_{ads,\ (111)} = E_{FA+-(111)} - E_{(111)} - E_{FA+}$, where $E_{FA+-(111)}$ is the total energy of the FA^+ adsorbed on the (111) facet of perovskite, $E_{(111)}$ is the (111) facet energy of perovskite, and E_{FA+} is the FA^+ cation energy; $E_{ads,\ BA+-(100)} = E_{FA+-(BA+-(100))} - E_{BA+-(100)} - E_{FA+}$, where $E_{FA+-(BA+-(100))}$ and $E_{BA+-(100)}$ is the total energy of the FA^+ adsorbed on the BA^+-bonded (100) facet of perovskite and the total energy of the BA^+ adsorbed on the (100) facet of perovskite, respectively; $E_{ads,\ BA+-(111)}$ =

$E_{FA+-(BA+-(111))}$–$E_{BA+-(111)}$–E_{FA+}, where $E_{FA+-(BA+-(111))}$ is the total energy of the FA^+ adsorbed on the BA^+-bonded (111) facet of perovskite.

The E_{ads} of H_2O molecule on the different facets is defined as $E_{ads,\ (100)} = E_{H2O\text{-}ads,\ (100)}$–$E_{(100)}$–$E_{H2O}$, where $E_{H2O\text{-}ads,\ (100)}$ is the total energy of the H_2O adsorbed on the (100) facet of perovskite, and E_{H2O} *is the energy of* H_2O molecule; $E_{ads,\ (111)} = E_{H2O\text{-}ads,\ (111)}$–$E_{(111)}$–$E_{H2O}$, where $E_{H2O\text{-}ads,\ (111)}$ is the total energy of the H_2O adsorbed on the (111) facet of perovskite.

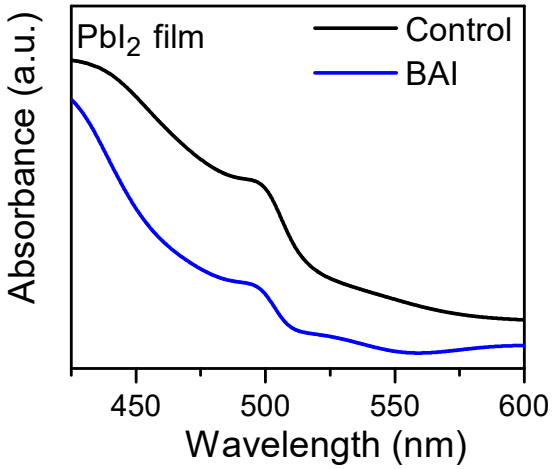

Fig. S1 UV–vis absorption spectra of the control and BAI-added PbI_2 films.

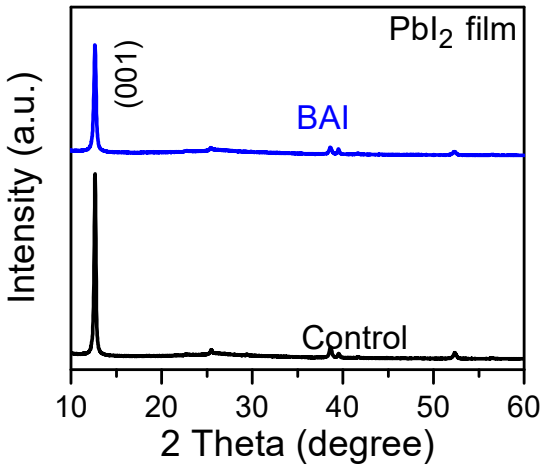

Fig. S2 XRD patterns of the control and BAI-added PbI_2 films.

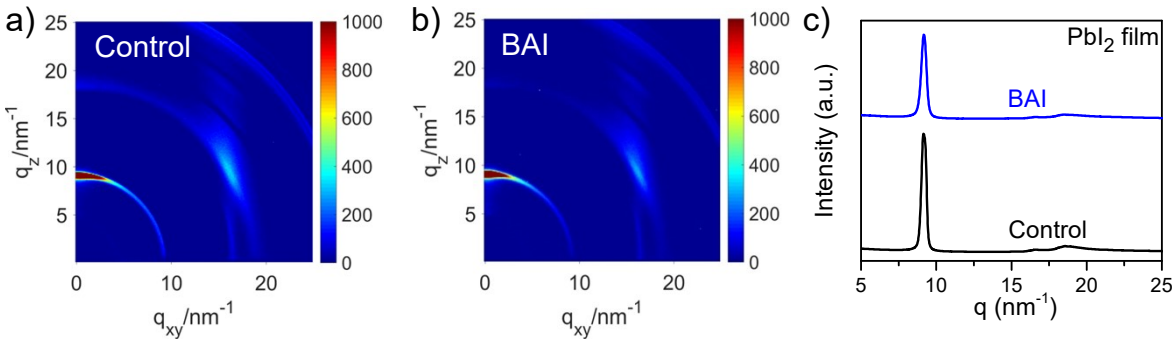

Fig. S3 GIWAXS patterns of a) the control and b) the BAI-added PbI_2 films. c) 1D patterns of the control and BAI-added PbI_2 films plotted based on GIWAXS results in a-b).

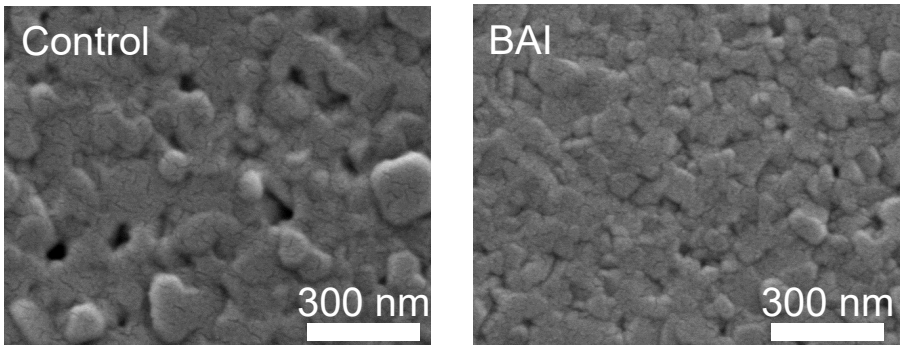

Fig. S4 Top-view SEM images of the control and BAI-added PbI_2 films.

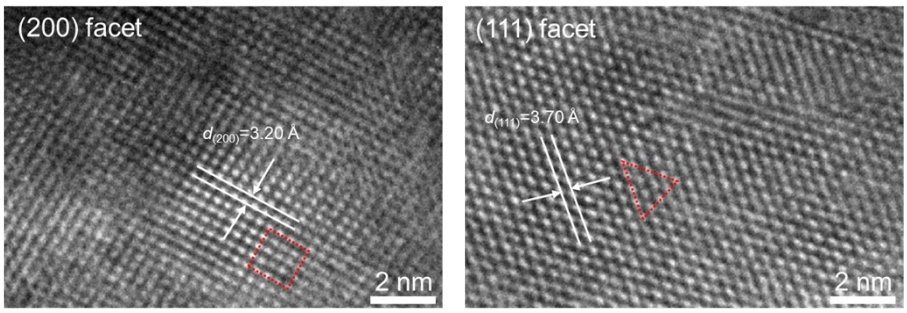

Fig. S5 HRTEM images of (200) facet and (111) facet of the perovskite; the embedded square and triangle represent the geometric features of (100) and (111) facets, respectively.

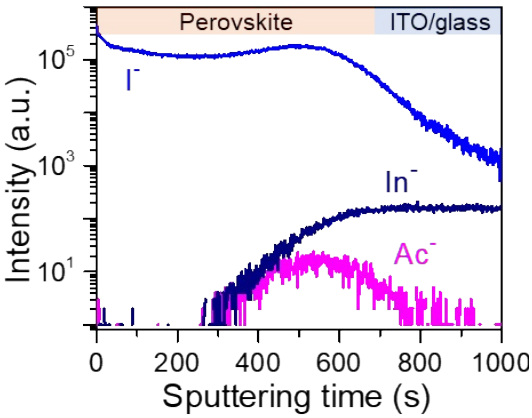

Fig. S6 ToF-SIMS spectra of Ac^-, I^- and In^- for the BAAc-based perovskite film.

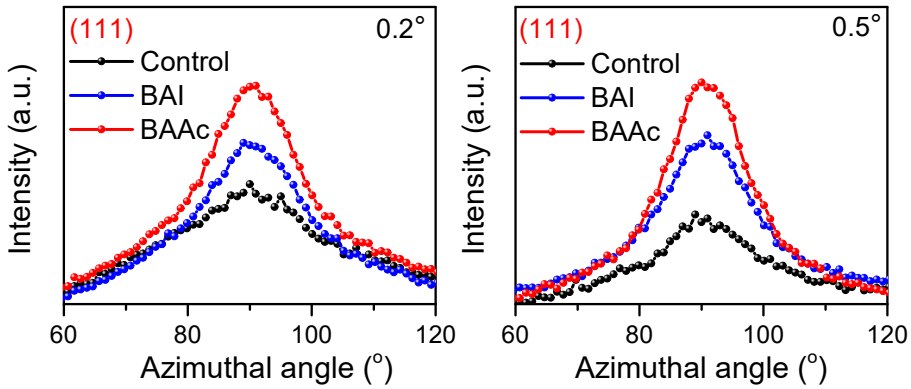

Fig. S7 Integrated intensities of the (111) facet of q_z at 17.5 nm^{-1} for the control, BAI- and BAAc-added perovskite films with the incident angles of 0.2° and 0.5°, plotted as a function of the azimuthal angle.

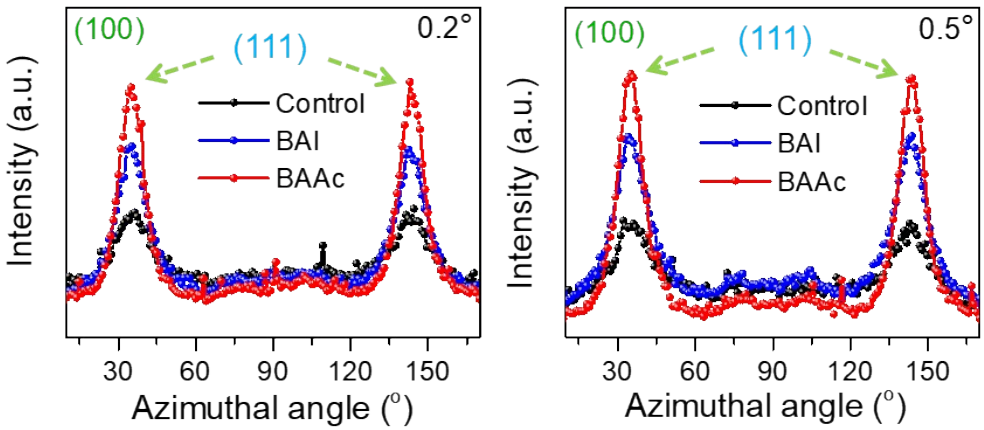

Fig. S8 Integrated intensities of the (100) facet of q_z at 10 nm^{-1} for the control, BAI- and BAAc-added perovskite films with the incident angles of 0.2° and 0.5°, plotted as a function of the azimuthal angle.

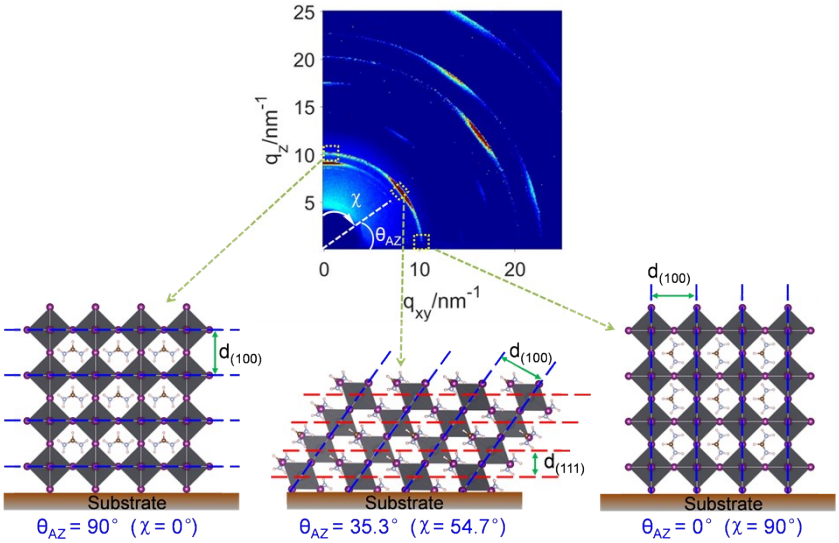

Fig. S9 Schematic illustration of the progression of the (100) facet orientation with the azimuthal angle (θ_{AZ}) in the GIWAXS pattern. At the azimuthal angle of 90° (χ=0°), the (100) facet is exposed and parallel to the substrate. When the azimuthal angle is 35.3° (χ=54.7°), the angle between the (100) facet and the substrate is 54.7° that is just the dihedral angle between the (100) and (111) facets. Therefore, in this circumstance the (111) facet is exposed and parallel to the substrate, appearing on the diffraction ring of the (100) facet.

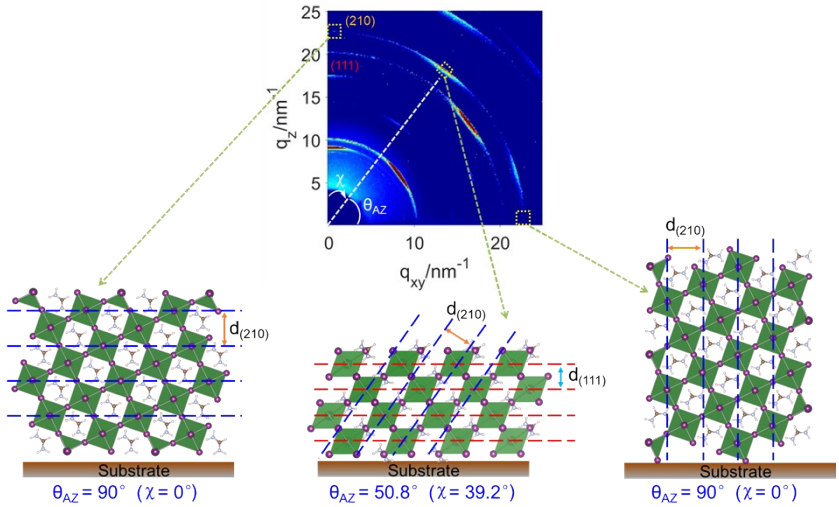

Fig. S10 Schematic illustration of the progression of the (210) facet orientation with the azimuthal angle (θ_{AZ}) in the GIWAXS pattern. At the θ_{AZ} of 90° (χ=0°), the (210) facet is exposed and parallel to the substrate. When the θ_{AZ} is 50.8° (χ=39.2°), the angle between the (210) facet and the substrate is 39.2° that is just the dihedral angle between the (111) and (210) facets, which is calculated according to a formula of

$\cos\theta=\frac{2\times1+1\times1}{\sqrt{2^2+1^2}\times\sqrt{1^2+1^2+1^2}}$. Therefore, in this circumstance the (111) facet is exposed and parallel to the substrate, appearing on the diffraction ring of the (210) facet.

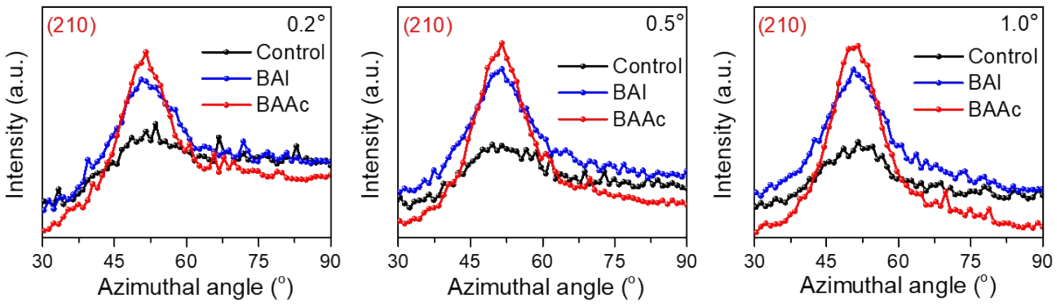

Fig. S11 Integrated intensities of the (210) facet of q_z at 23 nm^{-1} for the control, BAI- and BAAc-added perovskite films with the incident angles of 0.2°, 0.5° and 1.0°, plotted as a function of the azimuthal angle.

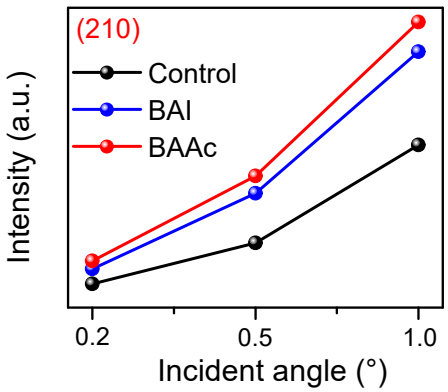

Fig. S12 Peak intensity of the azimuthal angle at 50.8° obtained from the (210) facets and plotted at different incident angles.

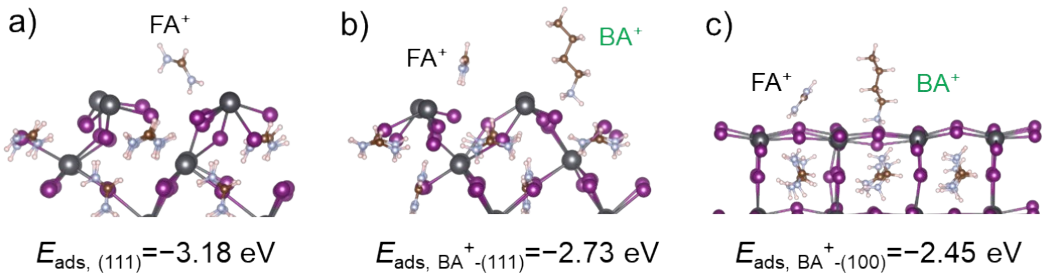

Fig. S13 Calculated adsorption energy (E_{ads}) of FA^+ adsorbed on the a) (111) facet ($E_{ads,\ (111)}$), b) BA^+-bonded (111) facet ($E_{ads,\ BA^+\text{-}(111)}$) and c) BA^+-bonded (100) facet ($E_{ads,\ BA^+\text{-}(100)}$) of $FAPbI_3$, respectively. Although BA^+ may also pre-bond to the (111) facet, it is much easier to bond with the (100) facet. This is because that compared to

I^-, positively charged Pb^{2+} and FA^+ are located on the more external layer of the (111) facet,[7] leading to the more difficult bonding with BA^+. In contrast, I^- on the (100) facet is exposed to the most outer layer, making it more likely to bond with BA^+. The calculated E_{ads} results also indicate that the $E_{ads,\ BA^+\text{-}(111)}$ is lower than $E_{ads,\ BA^+\text{-}(100)}$, suggesting FA^+ cations prefer to adsorb on the (111) facet.

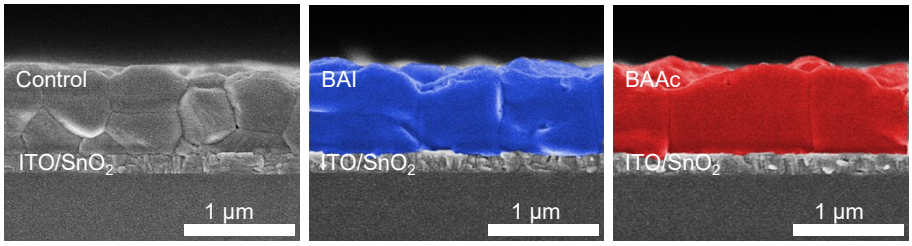

Fig. S14 Cross-sectional SEM images of the control, BAI- and BAAc-added perovskite films.

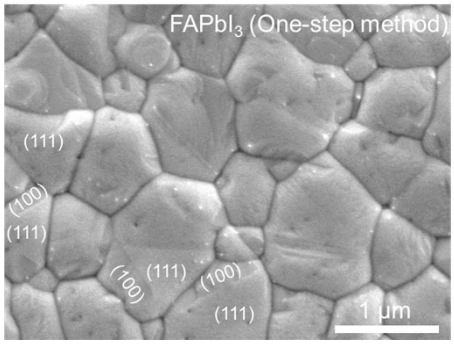

Fig. S15 Top-view SEM image of the $FAPbI_3$ perovskite film fabricated by the one-step method. In the one-step method, FAI, MABr, PbI_2 and $PbBr_2$ are simultaneously added into the precursor solution, where the molar ratio of FAI/MABr to PbI_2/$PbBr_2$ is 1:1, apart from chloride-based additives, favoring the formation of well-defined facets. In our study, the two-step method is employed for preparing perovskite films, where the excessive PbI_2 is often presented, largely influencing the morphology of the perovskite film. To validate our inference, we also fabricated perovskite films using the one-step method with a molar ratio of 1:1 between FAI/MABr and PbI_2/$PbBr_2$. As depicted in Fig. S15, we have also identified triangular facets within the perovskite film. Therefore, whether triangular or hexagon facets can be formed may depend on the different preparation methods of the perovskite film.

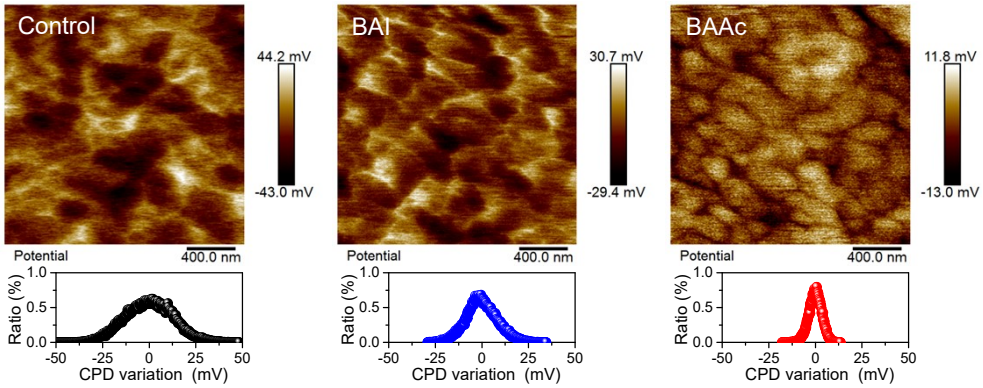

Fig. S16 KPFM images and potential distributions of the control, BAI- and BAAc-added perovskite films.

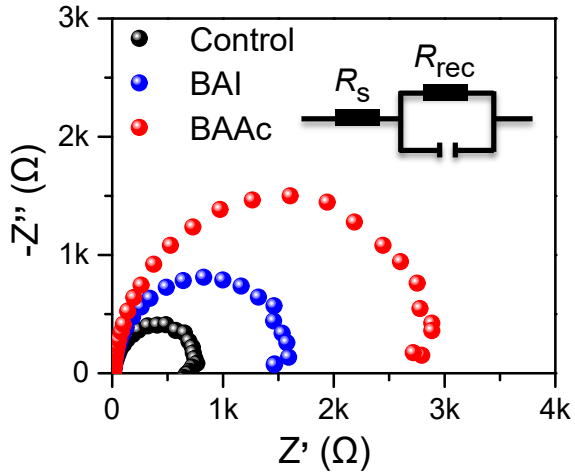

Fig. S17 Nyquist plots of PSCs with the control, BAI- and BAAc-added perovskite films; inset: corresponding equivalent circuit.

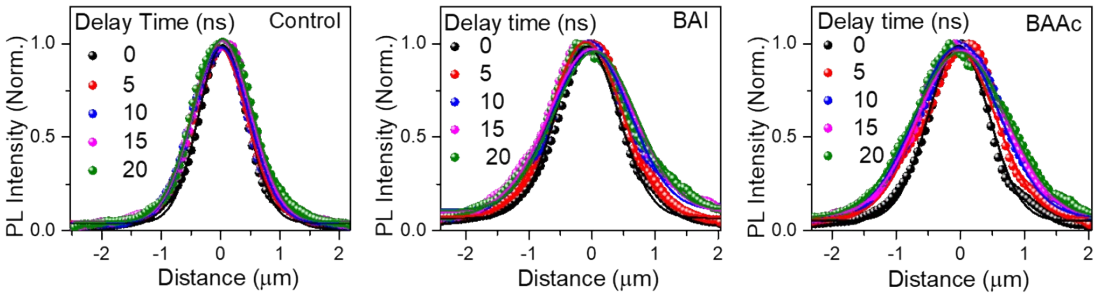

Fig. S18 Cross sections of the 2D PL intensity images of the control, BAI- and BAAc-added perovskite films along the x-axis fitted with Gaussian functions at different delay times based on normalized PL signal.

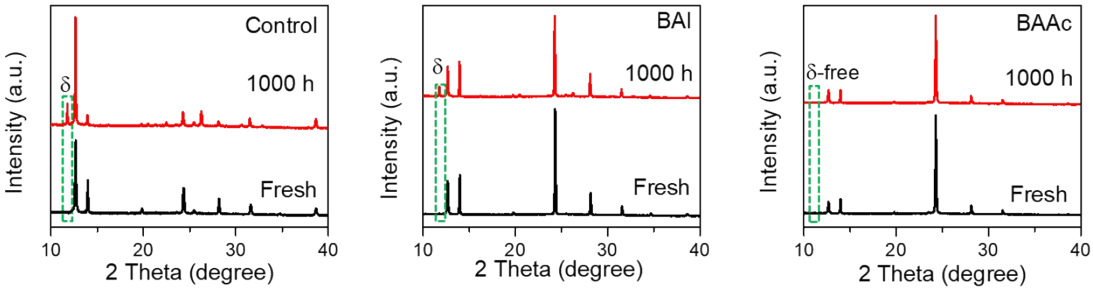

Fig. S19 XRD patterns of the control, BAI- and BAAc-added perovskite films aged under a RH of 40-50% at room temperature for 1000 h.

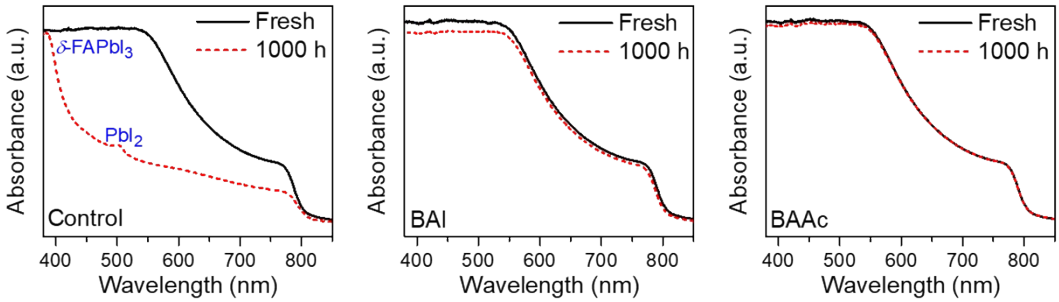

Fig. S20 UV-vis absorption spectra of the control, BAI- and BAAc-added perovskite films aged under a RH of 40-50% at room temperature for 1000 h.

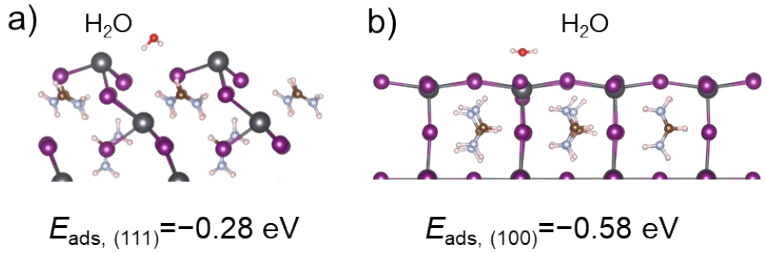

Fig. S21 Calculated adsorption energy (E_{ads}) of H_2O adsorbed on the a) (111) facet ($E_{ads, (111)}$), b) (100) facet ($E_{ads, (100)}$) of $FAPbI_3$, respectively.

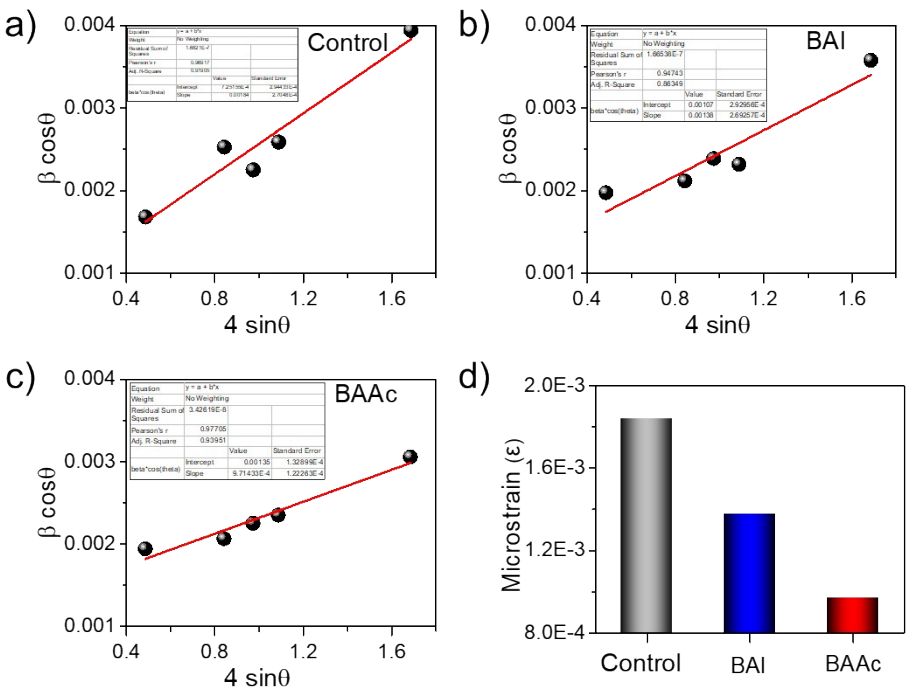

Fig. S22 a-c) Williamson−Hall plots and d) residual strain for the control, BAI- and BAAc-added perovskite films.

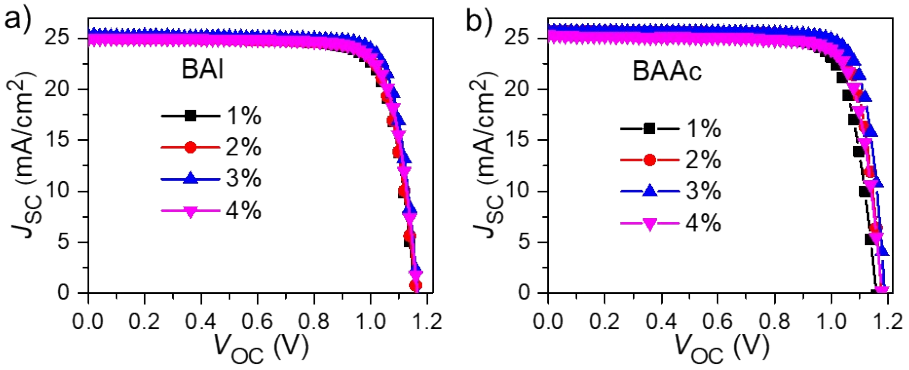

Fig. S23 *J–V* curves of the devices based on the perovskite films with different molar ratios of (a) BAI to PbI_2 and (b) BAAc to PbI_2.

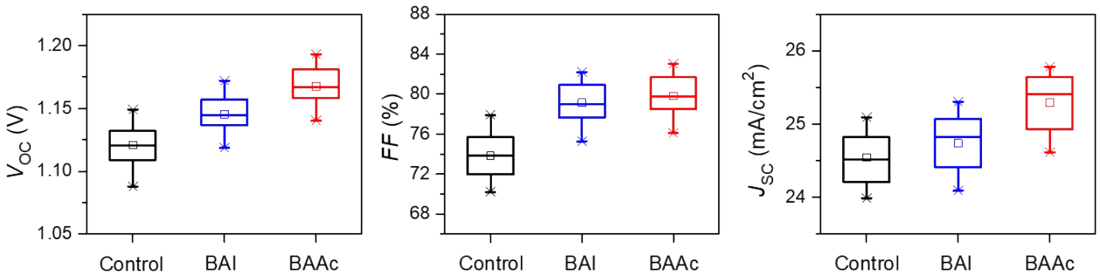

Fig. S24 Distributions of V_{OC}, *FF*, and J_{SC}, measured from 20 devices based on the control, BAI- and BAAc-added perovskite films.

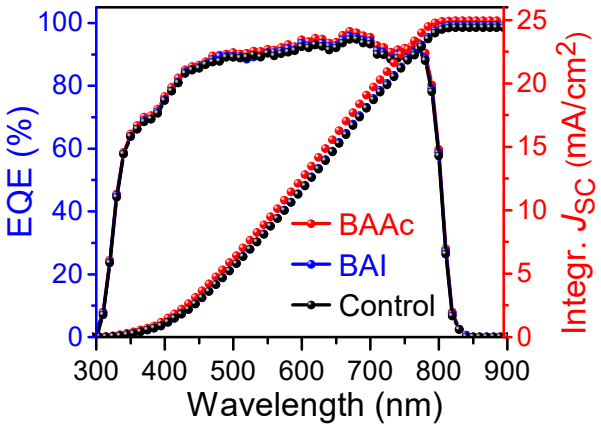

Fig. S25 EQE and integrated J_{SC} of the control, BAI- and BAAc-added PSCs.

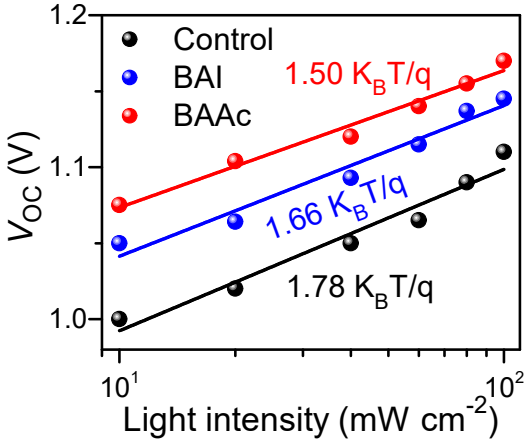

Fig. S26 V_{OC} dependence on light intensity curves for the control, BAI- and BAAc-added PSCs.

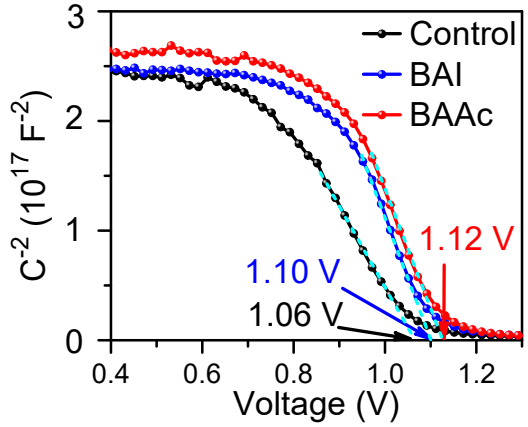

Fig. S27 The Mott-Schottky plots for the control, BAI- and BAAc-added PSCs.

Table S1 Carrier lifetimes of the control, BAI- and BAAc-added perovskite films.

Sample	A1 (%)	τ1 (ns)	A2 (%)	τ2 (ns)	τ_{ave} (ns)[a]
Control	26.56	76.28	73.44	1033.39	779.18
BAI	9.51	144.08	90.49	1532.67	1400.31
BAAc	8.16	160.92	91.84	2590.04	2391.82

[a] $\tau_{ave} = (\tau_1 \times A1 + t_2 \times A2)/(A1+A2)$.

Table S2 Detailed *J–V* parameters of the devices based on the perovskite films with different molar ratios of BAI to PbI_2.

Concentration of BAI	V_{OC} (V)	J_{SC} (mA/cm^2)	*FF* (%)	PCE (%)
1%	1.158	25.08	78.21	22.72
2%	1.163	25.10	79.31	23.15
3%	1.168	25.19	81.56	24.00
4%	1.165	24.97	79.24	23.05

Table S3 Detailed *J–V* parameters of the devices based on the perovskite films with different molar ratios of BAAc to PbI_2.

Concentration of BAAc	V_{OC} (V)	J_{SC} (mA/cm^2)	*FF* (%)	PCE (%)
1%	1.160	25.33	79.12	23.25
2%	1.178	25.62	81.46	24.61
3%	1.189	25.65	82.73	25.23
4%	1.181	25.31	79.90	23.90

Table S4 Detailed *J–V* parameters of the devices based on the control, BAI- and BAAc-added perovskite films with different scanning directions.

Device	V_{OC} (V)	J_{SC} (mA/cm^2)	*FF* (%)	PCE (%)	Hysteresis index (HI)[b]
Control (RS)	1.144	24.95	77.69	22.18 (21.05 ± 0.73)[a]	0.063
Control (FW)	1.129	24.68	74.58	20.78	
BAI (RS)	1.168	25.19	81.56	24.00 (22.95 ± 0.69)	0.037
BAI (FW)	1.161	25.00	79.64	23.11	
BAAc (RS)	1.189	25.65	82.73	25.23 (24.30 ± 0.62)	0.024
BAAc (FW)	1.180	25.38	82.27	24.64	

[a] Average PCEs obtained from 20 devices in parentheses; [b] $HI = (PCE_{RS} - PCE_{FW})/PCE_{RS}$.

Table S5 Summary of PCEs for reported devices based on (111) facet-dominated perovskite films in the literature.

Entry	V_{OC} (V)	J_{SC} (mA/cm^2)	*FF* (%)	PCE (%)	Year	Ref.
1	1.107	24.25	79.1	20.54	2019	8
2	1.106	25.09	82.95	22.03	2020	9[a]
3	1.18	24.4	79	22.7	2021	10[a]
4	1.14	23.82	81.14	22.03	2022	11
5	1.15	25.3	82	23.8	2023	12
6	1.16	24.49	77.85	22.09	2023	13
7	1.21	23.97	78.6	22.8	2024	14
8	1.189	25.65	82.73	25.23	2024	This work

[a] Dominated (111) facets in perovskite films were observed from the XRD results, but the two papers did not focus on the facet orientation.

References

1. W. Tian, C. Zhao, J. Leng, R. Cui, S. Jin, *J. Am. Chem. Soc.*, 2015, **137**, 12458-12461.
2. Z. Guo, J. S. Manser, Y. Wan, P. V. Kamat, L. Huang, *Nat. Commun.*, 2015, **6**, 7471.
3. G. Kresse, J. Furthmüller, *Phys. Rev. B*, 1996, **54**, 11169.
4. G. Kresse, D. Joubert, *Phys. Rev. B*, 1999, **59**, 1758.
5. J. P. Perdew, K. Burke, M. Ernzerhof, *Phys. Rev. Lett.*, 1997, **77**, 3865.
6. S. Grimme, J. Antony, S. Ehrlich, H. Krieg, *J. Chem. Phys.*, 2010, **132**, 154104.
7. L. Jing, X. Cheng, Y. Yuan, S. Du, J. Ding, H. Sun, X. Zhan, T. Zhou, *J. Phys. Chem. C*, 2019, **123**, 10826−10830.
8. K. Meng, X. Wang, Q. Xu, Z. Li, Z. Liu, L. Wu, Y. Hu, N. Liu, G. Chen, *Adv. Funct. Mater.*, 2019, **29**, 1902319.
9. H. Wang, Z. Wang, Z. Yang, Y. Xu, Y. Ding, L. Tan, C. Yi, Z. Zhang, K. Meng, G. Chen, Y. Zhao, Y. Luo, X. Zhang, A. Hagfeldt, J. Luo, *Adv. Mater.*, 2020, **32**, 2000865.
10. H. Zhang, M. Qin, Z. Chen, W. Yu, Z. Ren, K. Liu, J. Huang, Y. Zhang, Q. Liang, H. T. Chandran, P. W. K. Fong, Z. Zheng, X. Lu, G. Li, *Adv. Mater.*, 2021, **33**,

2100009,

11. X. Wang, Z. Han, F. Gao, C. Luo, Q. Zhao, *Sol. RRL*, 2022, **6**, 2100973.
12. C. Ma, F. T. Eickemeyer, S.-H. Lee, D.-H. Kang, S. J. Kwon, M. Grätzel, N.-G. Park, *Science*, 2023, **379**, 173–178.
13. X. Sun, D. Li, L. Zhao, Y. Zhang, Q. Hu, T. P. Russell, F. Liu, J. Wei, H. Li, *Adv. Mater.*, 2023, **35**, 2301115.
14. D. Li, X. Sun, Y. Zhang, Z. Guan, Y. Yue, Q. Wang, L. Zhao, F. Liu, J. Wei, H. Li, *Adv. Sci.*, 2024, **11**, 2401184.